AIA A JOURNAL
Vol. 31, No. 3, March 1993

Linearized Euler Predictions of Unsteady Aerodynamic Loads in Cascades

Kenneth C. Hall* and William S. Clark†
Duke University, Durham, North Carolina 27706

A linearized Euler solver for calculating unsteady flows in turbomachinery blade rows due to both incident gusts and vibratory blade motion is presented. Using the linearized Euler technique, one decomposes the flow into a mean (or steady) flow plus an unsteady, harmonically varying, small-disturbance flow. Linear variable coefficient equations describe the small-disturbance behavior of the flow and are solved using a pseudotime time-marching Lax-Wendroff scheme. For the blade-motion problem, a harmonically deforming computational grid that conforms to the motion of vibrating blades eliminates large error producing mean flow gradient terms that would otherwise appear in the unsteady flow tangency boundary condition. Also presented is a new, numerically exact, nonreflecting far-field boundary condition based on an eigenanalysis of the discretized equations. Computed flow solutions demonstrate the computational accuracy and efficiency of the present method. The solution of the linearized Euler equations requires one to two orders of magnitude less computer time than solution of the nonlinear Euler equations using traditional time-accurate time-marching techniques. Furthermore, it is shown that the deformable grid technique significantly improves the accuracy of the solution.

Introduction

UNSTEADY aerodynamic phenomena continue to produce serious aeroelastic problems in the development of new turbomachinery including turbopumps used in rocket propulsion and air-breathing turbomachines. These problems stem in part from an inability to model the unsteady aerodynamic behavior of cascades. Unsteady aerodynamic models must be able to accurately predict unsteady aerodynamic loads arising from blade motion and gust interaction. Furthermore, these models must be computationally efficient if they are to be part of a useful design system.

In recent years, several investigators have developed time-accurate time-marching Euler[1-6] and Navier-Stokes[7-10] solvers for analyzing unsteady flows in turbomachinery. These models are able to predict both small-disturbance (linear) and large-disturbance (nonlinear) unsteady flows in cascades. However, because of the large number of grid points required in these analyses and the requirement that the analyses be both accurate and stable, the maximum allowable time step used in the calculations must be small making these calculations prohibitively expensive for routine design use.

An alternative to the nonlinear time-marching appproach is the linearized technique. In a linearized analysis, the flow is assumed to be composed of a nonlinear mean (or steady) flow plus an unsteady, harmonically varying, small-perturbation flow. Linear variable-coefficient equations describe the unsteady perturbation flow. Although limited to small-disturbance flows, solution of the linearized unsteady flow equations require much less computational time than the solution of the full nonlinear unsteady flow equations.

Verdon et al.[11-14] and Whitehead and Grant[15] pioneered the development of linearized potential solvers for the blade-motion problem (that is, the flutter or aerodynamic damping problem). Later, Hall and Verdon[16] and Caruthers and Dalton[17] extended the linearized potential analysis to include the effect of incident vortical and entropic gusts using the flow decomposition technique of Atassi and Grzedzinski.[18] The linearized potential analyses, although computationally very efficient, are only applicable when the mean flow is irrotational and subsonic or weakly transonic.

The linearized Euler analysis—which is applicable to rotational, nonisentropic, transonic, small unsteady disturbance flows—was first introduced by Ni and Sisto.[19] Ni and Sisto used a pseudotime time-marching technique to solve the linearized harmonic Euler equations. However, initial results were confined to isentropic flows over flat-plate cascades. Hall and Crawley[20] later developed a direct method of solving the linearized Euler equations and applied the technique to realistic subsonic cascade geometries and transonic channel flows. For transonic flows, Hall and Crawley used shock fitting to model the motion of the shock. Although shock fitting does provide sharp, clearly defined shocks and shock motions, it is cumbersome and complex and, therefore, less desirable than shock capturing. In a recent paper, Lindquist and Giles[21] outlined the conditions under which shock capturing correctly models shock motion in a linearized Euler analysis. The linearized Euler technique has shown the potential for dramatically reducing the computational cost required to solve unsteady subsonic and transonic flow problems in both two and three dimensions while still modeling the dominant physics of the unsteady flow problem.[20,22]

Although several nonlinear time-marching Euler codes have been developed that use moving or deforming computational grids,[23-26] most previous linearized potential and Euler solvers have used computational grids fixed in space for solution of the linearized equations.[12-14,20] To calculate the flutter stability of an airfoil, one assumes that the blades vibrate with a fixed amplitude, frequency, and interblade phase angle. The linearized equations are then solved to determine the unsteady pressure on the airfoil surface. However, since the blades vibrate through the stationary grid, the boundary conditions that apply at the instantaneous location of the airfoil must be extrapolated back to the mean location of the airfoil where the boundary conditions are actually applied. Similarly, once the unsteady flow solution has been found on the fixed grid, terms involving the mean flow pressure gradient must be added to the unsteady pressure at the mean blade location to obtain the

---

Presented as Paper 91-3378 at the AIAA/SAE/ASME/ASEE 27th Joint Propulsion Conference, Sacramento, CA, June 24-27, 1991; received July 12, 1991; revision received July 17, 1992; accepted for publication July 20, 1992.

*Assistant Professor, Department of Mechanical Engineering and Materials Science. Member AIAA.

†Research Assistant, Department of Mechanical Engineering and Materials Science. Member AIAA.

unsteady pressure at the instantaneous position of the blade. These gradient terms are difficult to evaluate accurately in practice, especially near the leading edges of fan and compressor blades. The resulting errors introduced at the airfoil boundary make the computed solution of unsteady aerodynamic loads on moving airfoils inaccurate and sensitive to small errors in the computed steady flowfield.

To overcome some of the difficulties associated with fixed grid potential calculations, Whitehead and Grant[15] introduced a linearized potential transformation that can be viewed as a rigid-body motion of the grid. Because the grid in effect moves with the airfoil, the scheme does not require extrapolation terms at the airfoil boundaries. Although this approach allows rigid-body motions of airfoils to be analyzed, flexible mode shapes, which are common in turbomachinery aeroelasticity, cannot be analyzed. Recently, Hall[27] developed a linearized potential analysis that uses a deforming grid and is capable of analyzing both rigid-body and elastic airfoil motions.

This paper presents a deforming grid linearized Euler solver that is suitable for the aerodynamic portion of the forced response analysis of turbomachinery blades. The paper addresses two problems: the gust response problem, where a nonvibrating row of airfoils interacts with a wake from an upstream blade row; and the aerodynamic damping problem, where vibration of the airfoils themselves induces aerodynamic loads. It is demonstrated that the use of a deforming grid results in significantly more accurate predictions of the unsteady flowfield and aerodynamic loads. Furthermore, because the grid deforms elastically, the method can analyze both rigid-body and flexible blade motions.

This paper also presents a new, numerically exact, nonreflecting far-field boundary condition. Unsteady flow computations require nonreflecting far-field boundaries to prevent spurious reflections that would otherwise corrupt the solution. Previous investigators have found the exact analytical behavior of the linearized potential[11,15] and the linearized Euler[20] equations and matched these analytical solutions to numerical solutions at the far-field boundary. This paper presents an alternative approach. The exact far-field behavior of the discretized equations is found from an eigenanalysis. The resulting eigenmodes are used to construct numerically exact, two-dimensional nonreflecting boundary conditions.

Results of the linearized Euler analysis demonstrate the accuracy and efficiency of the method. The computed results agree well with analytical flat-plate results for both gust response and aerodynamic damping problems. Calculations of unsteady flows through a typical compressor blade row show the ability of the method to analyze unsteady subsonic and transonic flowfields about loaded airfoils. Finally, it is shown that the method is very efficient; typically, the method requires one to two orders of magnitude less computer time than nonlinear time-marching algorithms.

Theoretical Approach

Flowfield Description

Although viscous forces produce the wakes that are a prime source of forced response in turbomachinery, inviscid effects dominate the resulting wake interaction with a downstream blade row so long as the flow remains attached and the boundary layers are thin. Therefore, in the present analysis, the fluid flow through a single row of airfoils is modeled as two-dimensional, adiabatic, and inviscid. The governing equations of fluid motion are then the two-dimensional Euler equations, which in differential form are given by

$$\frac{\partial \hat{U}}{\partial t} + \frac{\partial \hat{F}}{\partial x} + \frac{\partial \hat{G}}{\partial y} = 0 \tag{1}$$

Here $\hat{U}$ is the vector of conservation variables and $\hat{F}$ and $\hat{G}$ are flux vectors given by

$$\hat{U} = \begin{bmatrix} \hat{\rho} \\ \hat{\rho}\hat{u} \\ \hat{\rho}\hat{v} \\ \hat{e} \end{bmatrix}, \quad \hat{F} = \begin{bmatrix} \rho\hat{u} \\ \hat{\rho}\hat{u}^2 + \hat{p} \\ \hat{\rho}\hat{u}\hat{v} \\ \hat{\rho}\hat{u}\hat{h}_0 \end{bmatrix}, \quad \hat{G} = \begin{bmatrix} \rho\hat{v} \\ \hat{\rho}\hat{u}\hat{v} \\ \hat{\rho}\hat{v}^2 + \hat{p} \\ \hat{\rho}\hat{v}\hat{h}_0 \end{bmatrix}$$

where $\hat{\rho}$ is the density, $\hat{u}$ and $\hat{v}$ are the x and y components of the velocity (i.e., components in the axial and circumferential directions), $\hat{e}$ is the total internal energy, and $\hat{h}_0$ is the total enthalpy. For an ideal gas with constant specific heats, the total enthalpy is

$$\hat{h}_0 = \frac{\hat{e} + \hat{p}}{\hat{\rho}} = \frac{\gamma}{\gamma - 1}\frac{\hat{p}}{\hat{\rho}} + \tfrac{1}{2}(\hat{u}^2 + \hat{v}^2)$$

where $\hat{p}$ is the static pressure and γ the ratio of specific heats.

For numerical integration using finite volume schemes, it will be convenient to use the integral form of Eq. (1) that applies to a time-varying control volume D. If the x and y components of velocity of the surface of the control volume ∂D are f_t and g_t, respectively, then the integral statement of continuity of mass, momentum, and energy is

$$\frac{\mathrm{d}}{\mathrm{d}t}\iint_D \hat{U}\,\mathrm{d}x\,\mathrm{d}y + \oint_{\partial D} (\hat{F} - f_t\hat{U})\,\mathrm{d}y - \oint_{\partial D} (\hat{G} - g_t\hat{U})\,\mathrm{d}x = 0 \tag{2}$$

To solve for the nonlinear time-dependent behavior of the flow requires that the Euler equations be time marched in a time-accurate fashion. Such calculations are notoriously expensive. Fortunately, for many unsteady flows of interest to aeroelasticians, the amplitude of unsteadiness of the flow is small compared to the mean flow. Therefore, one can approximate the unsteady flowfield as the sum of a nonlinear mean flow plus a small-perturbation unsteady flow. The amplitude of the unsteady perturbation will be of the same order as the amplitude of the blade motion for the aerodynamic damping problem or the amplitude of the wake disturbance for the gust-response problem.

For the aerodynamic damping problem, we define a harmonically deforming computational grid that conforms to the motion of the airfoil. The computational coordinate system ξ, η is to zeroth order the same as the physical coordinate system x, y. To first order, it differs by a harmonically varying small perturbation, i.e.,

$$x(\xi,\eta,\tau) = \xi + f(\xi,\eta)e^{j\omega\tau} \tag{3}$$

$$y(\xi,\eta,\tau) = \eta + g(\xi,\eta)e^{j\omega\tau} \tag{4}$$

$$t(\xi,\eta,\tau) = \tau \tag{5}$$

where ω is the frequency of blade motion. The first-order complex perturbation functions f and g describe how the grid deforms in physical space and are chosen so that the boundary of the grid conforms to the motion of the airfoils. Note that this formulation allows for both rigid-body and elastic blade deformations. Shown in Fig. 1 is a typical computational grid for the case of a cascade of airfoils pitching about their midchords with an interblade phase angle σ of − 180 deg. In the physical coordinate system, the grid appears to deform harmonically; in the computational coordinate system, the grid appears stationary and undeformed.

Having defined the computational coordinate system, the unsteady flowfield is now represented by the two-term perturbation series

$$\hat{U}(\xi,\eta,\tau) = U(\xi,\eta) + u(\xi,\eta)e^{j\omega\tau} \tag{6}$$

where U is the vector of conservation variables representing the mean background flow and u the vector of complex perturbation amplitudes of the conservation variables. Note that we define the perturbation series in the computational rather than the physical coordinate system. Hence, the unsteadiness in the flow as seen in the physical coordinate system arises from both the perturbation quantities u and the spatial deformation of the nonuniform steady flowfield U.

In a similar fashion, the flux vectors are expanded in a perturbation series. Taylor expanding the flux vectors about the mean flow gives to first order

$$\hat{F}(\xi,\eta,\tau) = F(\xi,\eta) + \frac{\partial F}{\partial U} u(\xi,\eta) e^{j\omega\tau} \tag{7}$$

$$\hat{G}(\xi,\eta,\tau) = G(\xi,\eta) + \frac{\partial G}{\partial U} u(\xi,\eta) e^{j\omega\tau} \tag{8}$$

The Jacobians $\partial F/\partial U$ and $\partial G/\partial U$ are evaluated using the mean flow solution U and are given by

$$\frac{\partial F}{\partial U} = \begin{bmatrix} 0 & 1 & 0 & 0 \\ \frac{(\gamma-3)}{2} U^2 + \frac{(\gamma-1)}{2} V^2 & -(\gamma-1)U & -(\gamma-3)V & \gamma-1 \\ -UV & V & U & 0 \\ U\left(\frac{\gamma-1}{2} V_T^2 - h_0\right) & h_0 - (\gamma-1)U^2 & -(\gamma-1)UV & \gamma U \end{bmatrix}$$

and

$$\frac{\partial G}{\partial U} = \begin{bmatrix} 0 & 0 & 1 & 0 \\ -UV & V & U & 0 \\ \frac{\gamma-3}{2} V^2 + \frac{\gamma-1}{2} U^2 & -(\gamma-1)U & -(\gamma-3)V & \gamma-1 \\ V\left(\frac{\gamma-1}{2} V_T^2 - h_0\right) & -(\gamma-1)UV & h_0 - (\gamma-1)V^2 & \gamma V \end{bmatrix}$$

where $V_T^2 = U^2 + V^2$.

This form of perturbation analysis, where the perturbation is taken about a coordinate system moving with the airfoil, closely resembles the method of strained coordinates due to Lighthill for analyzing singular perturbation problems.[28] Since the present problem is, strictly speaking, a regular perturbation problem, the proposed coordinate straining is not required to formulate the problem. Nevertheless, using strained coordinates eliminates troublesome mean flow gradient terms that would otherwise appear in the flow tangency boundary conditions and the evaluation of the unsteady surface pressure, greatly improving the accuracy of the method.

Next, we express the temporal and spatial derivatives in the physical coordinate system in terms of the temporal and spatial derivatives in the computational coordinate system. To first order,

$$\frac{\partial}{\partial x} = \frac{\partial}{\partial \xi} - \left(\frac{\partial f}{\partial \xi}\frac{\partial}{\partial \xi} + \frac{\partial g}{\partial \xi}\frac{\partial}{\partial \eta}\right) \tag{9}$$

$$\frac{\partial}{\partial y} = \frac{\partial}{\partial \eta} - \left(\frac{\partial f}{\partial \eta}\frac{\partial}{\partial \xi} + \frac{\partial g}{\partial \eta}\frac{\partial}{\partial \eta}\right) \tag{10}$$

$$\frac{\partial}{\partial t} = \frac{\partial}{\partial \tau} - j\omega\left(f\frac{\partial}{\partial \xi} + g\frac{\partial}{\partial \eta}\right) \tag{11}$$

The first term on the right-hand side of each equation represents the zeroth-order part of the operator whereas the second term represents the first-order part.

Having defined the computational coordinate system and the perturbation series expansion of the flow variables, the conservation variables, the flux vectors, and the differential operators, (6–8) are substituted into the nonlinear Euler equations, (1). Making use of Eqs. (9–11), the Euler equations are expanded in a perturbation series. Collecting terms of zeroth and first order gives the mean flow and linearized Euler equations, respectively, i.e.,

$$\frac{\partial F}{\partial \xi} + \frac{\partial G}{\partial \eta} = 0 \tag{12}$$

and

$$\begin{aligned} j\omega u + \frac{\partial}{\partial \xi}\frac{\partial F}{\partial U} u + \frac{\partial}{\partial \eta}\frac{\partial G}{\partial U} u &= j\omega\left(f\frac{\partial}{\partial \xi} + g\frac{\partial}{\partial \eta}\right) U \\ &+ \left(\frac{\partial f}{\partial \xi}\frac{\partial}{\partial \xi} + \frac{\partial g}{\partial \xi}\frac{\partial}{\partial \eta}\right) F + \left(\frac{\partial f}{\partial \eta}\frac{\partial}{\partial \xi} + \frac{\partial g}{\partial \eta}\frac{\partial}{\partial \eta}\right) G \end{aligned} \tag{13}$$

The general solution procedure is to first solve for the mean flow. The mean flow equations are nonlinear in the mean flow conservation variables U. The resulting steady solution is used to form the Jacobians that appear in the linearized Euler equations (13), as well as the mean fluxes. The linearized equations are then solved for the perturbation flow u. Note that the linearized Euler equations contain the homogeneous term $j\omega u$, which represents the time rate of change of the perturbed conservation variables. Since the Jacobians are real, it is this term that couples the real and imaginary parts of the perturbation flow. Equation (13) also contains an inhomogeneous term (the right-hand side) that is a function of the known steady flow and the prescribed grid motion. For the gust-response problem, the inhomogeneous term is identically zero since the computational grid is nondeforming.

For numerical integration of Eqs. (12) and (13), it is convenient to make the mean flow variables U and the perturbation variables u artificially time dependent. As suggested by Ni and Sisto,[19] we let

$$\hat{U}(\xi,\eta,\tau) = U(\xi,\eta,\tau) + u(\xi,\eta,\tau) e^{j\omega t} \tag{14}$$

Substitution of this assumption into the nonlinear Euler equations (1) and again collecting terms of equal order gives

$$\frac{\partial U}{\partial \tau} + \frac{\partial F}{\partial \xi} + \frac{\partial G}{\partial \eta} = 0 \tag{15}$$

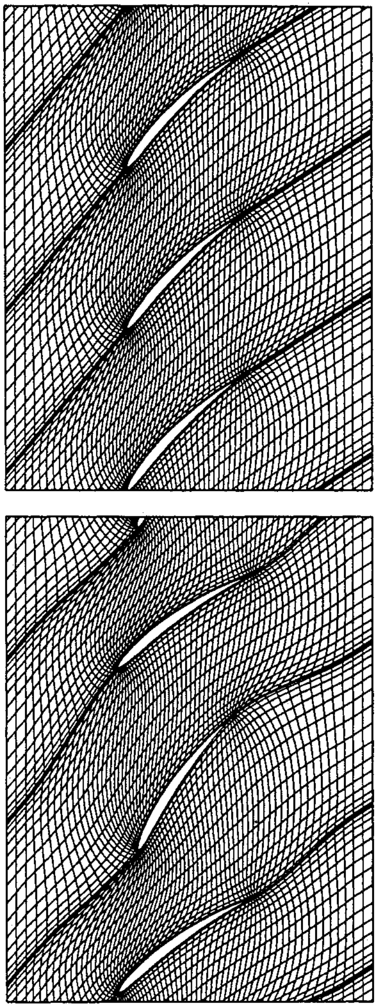

Fig. 1 Top: Grid in computational coordinate system ξ, η (tenth standard configuration cascade). Bottom: Grid in physical coordinate system x,y for the case of a cascade of airfoils pitching about their midchords with interblade phase angle $\sigma = -180$ deg.

and

$$\frac{\partial \boldsymbol{u}}{\partial \tau} + j\omega \boldsymbol{u} + \frac{\partial}{\partial \xi}\frac{\partial \boldsymbol{F}}{\partial \boldsymbol{U}}\boldsymbol{u} + \frac{\partial}{\partial \eta}\frac{\partial \boldsymbol{G}}{\partial \boldsymbol{U}}\boldsymbol{u} = j\omega\left(f\frac{\partial}{\partial \xi} + g\frac{\partial}{\partial \eta}\right)\boldsymbol{U} + \left(\frac{\partial f}{\partial \xi}\frac{\partial}{\partial \xi} + \frac{\partial g}{\partial \xi}\frac{\partial}{\partial \eta}\right)\boldsymbol{F} + \left(\frac{\partial f}{\partial \eta}\frac{\partial}{\partial \xi} + \frac{\partial g}{\partial \eta}\frac{\partial}{\partial \eta}\right)\boldsymbol{G} \tag{16}$$

Now both the nonlinear mean flow equations and the linearized Euler equations contain explicit time-derivative terms making the equations hyperbolic in time. This allows solution of the equations using conventional time-marching algorithms. The equations are marched in time until the conservation variables reach their steady-state values. Hence, the time-derivative terms in Eqs. (15) and (16) are driven to zero and the original steady nonlinear and linearized unsteady Euler equations (12) and (13) are recovered. Furthermore, because we are only interested in steady-state values of $\boldsymbol{U}$ and $\boldsymbol{u}$, there is no need to time march the equations time accurately; multiple-grid and local time stepping acceleration techniques are used, greatly reducing the computational time required to solve an unsteady flow problem.

For finite volume calculations, the integral form of Eq. (16) is preferred. The integral form may be found either by direct integration of the differential form [Eq. (16)] or by linearizing Eq. (2). In any event, the resulting linearized integral statement of conservation of mass, momentum, and energy is given by

$$\frac{\mathrm{d}}{\mathrm{d}\tau}\iint_D \boldsymbol{u}\,\mathrm{d}\xi\,\mathrm{d}\eta + j\omega\iint_D \boldsymbol{u}\,\mathrm{d}\xi\,\mathrm{d}\eta + \oint_{\partial D}\left(\frac{\partial \boldsymbol{F}}{\partial \boldsymbol{u}}\boldsymbol{u}\,\mathrm{d}\eta - \frac{\partial \boldsymbol{G}}{\partial \boldsymbol{U}}\boldsymbol{u}\,\mathrm{d}\xi\right) = -j\omega\iint_D \boldsymbol{U}(\mathrm{d}\xi\,\mathrm{d}g + \mathrm{d}f\,\mathrm{d}\eta) + j\omega\oint_{\partial D}(f\boldsymbol{U}\,\mathrm{d}\eta - g\boldsymbol{U}\,\mathrm{d}\xi) - \oint_{\partial D}(\boldsymbol{F}\,\mathrm{d}g - \boldsymbol{G}\,\mathrm{d}f) \tag{17}$$

Unsteady Boundary Conditions

To complete the specification of the fluid flow problem, boundary conditions must be specified around the entire computational domain. Since the linearized unsteady flow problem is of interest and the boundary conditions for steady flow solvers are well known, we will present only the unsteady flow boundary conditions. The discussion of far-field boundary conditions is deferred until the section describing the numerical algorithm.

Flow Tangency

Suppose the vector $\hat{\boldsymbol{R}}(s,\tau)$ describes the location of the surface of the reference airfoil at time τ, where s is the distance along the airfoil surface. The assumption of small-amplitude harmonic blade motion allows a perturbation series representation of the position vector, i.e.,

$$\hat{\boldsymbol{R}}(s,\tau) = \boldsymbol{R}(s,\tau) + \boldsymbol{r}(s)e^{j\omega\tau} \tag{18}$$

Substitution of Eq. (18) into the nonlinear flow tangency condition leads to the first-order unsteady flow tangency condition

$$\boldsymbol{v}\cdot\boldsymbol{n} = j\omega\boldsymbol{r}\cdot\boldsymbol{n} + \boldsymbol{V}\cdot\boldsymbol{s}\frac{\partial \boldsymbol{r}}{\partial s}\cdot\boldsymbol{n} \tag{19}$$

where $\boldsymbol{V}$ and $\boldsymbol{v}$ are the mean flow and perturbation flow velocities, respectively, and $\boldsymbol{n}$ and $\boldsymbol{s}$ are unit vectors normal and tangent to the mean surface of the airfoil. The first term on the right-hand side of Eq. (19) represents the upwash due to airfoil translation. The second term represents the upwash due to the local rotation of the airfoil surface. Note that unlike fixed grid calculations, the present analysis does not require any extrapolation terms since the grid moves with the airfoil.

Periodic Boundary Conditions

Because linear equations describe the unsteady perturbation flow, we may superpose solutions. Without loss of generality, then, it is assumed that the solution is spatially periodic with interblade phase angle σ. Therefore, upstream and downstream of the airfoil along the so-called periodic boundaries, the boundary conditions take the form

$$\boldsymbol{u}(\xi,\eta + G) = \boldsymbol{u}(\xi,\eta)e^{j\sigma} \tag{20}$$

where G is the blade-to-blade gap. The assumption of complex periodicity allows the computational domain to be reduced to a single blade passage.

Numerical Algorithm

Grid Generation

The computational grids used in the present investigation are H grids. Although useful for steady flow calculations, C grids and O grids lack the resolution in the far-field region to resolve short wavelength unsteady acoustic, vortical, and entropic waves. Furthermore, rapid changes in grid resolution can produce spurious reflections or attenuation of waves, corrupting the unsteady solution. H grids provide good resolution throughout the computational domain and, therefore, are the natural choice for unsteady flow calculations. The present analysis uses the same computational grid for both the steady and unsteady flow calculations. The grid is generated for a single blade passage using an algorithm based on the elliptic grid generation technique due to Thompson et al.[29]

For unsteady flows due to blade motion, the unsteady grid motion perturbations f and g must be defined. These perturbation functions are somewhat arbitrary, although for computational accuracy, one would like f and g to be smooth functions. Therefore, we use Laplace's equation to describe the behavior of the grid motion perturbation on the interior of the grid. A finite element technique is used to discretize $\nabla^2 f = 0$ and $\nabla^2 g = 0$ on the steady computational grid. Dirichlet boundary conditions are specified on the boundary of the computational domain. These boundary conditions are chosen so that the motion of the grid conforms to the motion of the airfoils, satisfies complex perodicity across the periodic and wake boundaries, and goes to zero in the upstream and downstream far fields. The last requirement is made to simplify the implementation of the far-field boundary conditions. The discretized equations are solved directly using lower-upper decomposition with back substitution. Figure 1 shows a typical computational grid and corresponding unsteady grid deformation for the case of a cascade of compressor airfoils pitching about their midchords with an interblade phase angle σ of -180 deg.

Lax-Wendroff Integration Scheme

Both the steady and unsteady flowfields are computed by time marching the pseudotime-dependent Euler equations (15) and (16) to steady state using Ni's Lax-Wendroff technique.[30,31] Local time stepping and the multiple-grid technique are used to accelerate convergence to steady state. The steady flowfield is solved first and the solution saved for use in the unsteady flow calculations.

Ni's Lax-Wendroff scheme can be easily applied to the linearized Euler equations with some minor modifications. To illustrate, recall that the Lax-Wendroff scheme is based on the Taylor series approximation

$$\delta u = u^{n+1} - u^n = \Delta\tau \frac{\partial u^n}{\partial t} + {}^1\!/\!_2 \Delta\tau^2 \frac{\partial^2 u^n}{\partial \tau^2} \tag{21}$$

where $\Delta\tau$ is the time step and n denotes the nth time step. Substitution of Eq. (16) into Eq. (21) gives

$$\delta u = \Delta u - {}^1\!/\!_2 \Delta\tau \left(j\omega\Delta u + \frac{\partial}{\partial \xi}\frac{\partial F}{\partial U}\Delta u + \frac{\partial}{\partial \eta}\frac{\partial G}{\partial U}\Delta u \right) \tag{22}$$

where

$$\begin{aligned} \Delta u &= \Delta\tau \frac{\partial u^n}{\partial \tau} \\ &= -\Delta\tau \left(j\omega u^n + \frac{\partial}{\partial \xi}\frac{\partial F}{\partial U} u^n + \frac{\partial}{\partial \eta}\frac{\partial G}{\partial U} u^n - b \right) \end{aligned} \tag{23}$$

Here $\boldsymbol{b}$ is a shorthand notation for the right-hand side of Eq. (16). The right-hand sides of Eqs. (22) and (23) are approximated using conservative finite volume operators. The steady flow solution is used to form the Jacobians $\partial F/\partial U$ and $\partial G/\partial U$ and the inhomogeneous term $\boldsymbol{b}$. Since these quantitites do not vary with time, they are calculated once just before the start of the iteration procedure. Note that the homogeneous source terms $j\omega u$ and $j\omega\Delta u$ couple the real and imaginary parts of the solution. A mixture of second-difference and fourth-difference smoothing is used to eliminate spurious sawtooth modes and to capture shocks.

Far-Field Nonreflecting Boundary Conditions

Unsteady flow computations require nonreflecting boundary conditions at the far-field boundaries to prevent spurious reflections of outgoing waves. This section outlines a new, numerically exact, nonreflecting boundary treatment for the *discretized* small-disturbance equations.

The computational grid used in the present analysis is an H-grid with I nodes in the axial direction and J nodes in the circumferential direction. Although the solution of the linearized Euler equations are found through an iterative rather than a direct method, the converged solution may be thought of as satisfying a large sparse matrix equation of the form

$$\begin{bmatrix} B_1 & C_1 & & & \\ A_2 & B_2 & C_2 & & \\ & \ddots & \ddots & \ddots & \\ & & A_{I-1} & B_{I-1} & C_{I-1} \\ & & & A_I & B_I \end{bmatrix} \begin{Bmatrix} u_1 \\ u_2 \\ \vdots \\ u_{I-1} \\ u_I \end{Bmatrix} = \begin{Bmatrix} b_1 \\ b_2 \\ \vdots \\ b_{I-1} \\ b_I \end{Bmatrix} \tag{24}$$

where $\boldsymbol{u}_i$ is the vector of perturbation variables along the ith grid line in the axial direction, and $\boldsymbol{b}_i$ is the vector of inhomogeneous terms arising from the motion of the grid and the imposition of blade motion or wake excitations. The submatrices $[A_i]$, $[B_i]$, and $[C_i]$ are large sparse matrices, each of size $4J \times 4J$, that depend on the details of the finite volume integration algorithm. For the Ni scheme with second-difference smoothing, the submatrices $[A_i]$, $[B_i]$, and $[C_i]$ are block tridiagonal, the blocks being 4×4 matrices. Upstream and downstream of the blade row where periodic boundary conditions are applied, 4×4 blocks also appear in the upper right and lower left corners of the submatrices. The entries of these matrices would change somewhat if a different discretization scheme were used, but the form would be similar.

For the moment, consider the case where no far-field disturbances are imposed. If in the far-field the grid spacing in the axial direction is uniform, the "streamline" grid lines are parallel and straight, and the grid does not deform, then the discretized equations are identical from axial station to axial station. (Downstream the "streamline" grid lines must also be aligned with the steady flowfield.) The discretized equations at the ith axial station in the far field take the form

$$[A]\{u_{i-1}\} + [B]\{u_i\} + [C]\{u_{i+1}\} = 0 \tag{25}$$

where now the matrices $[A]$, $[B]$, and $[C]$ are independent of i. Because the equations are linear and the same from station to station, a solution which satisfies the discretized far-field equations at the ith station would also satisfy the equations at any other far-field station. This, along with the insight that we want to model the motion of waves in the far field, suggests that we hypothesize that the solution in the far field is of the form

$$\{u_i\} = \sum_m z_m^i \{\bar{u}_m\} w_m \tag{26}$$

where $\boldsymbol{u}_i$ is the solution at the ith station, z_m is an eigenvalue, $\bar{\boldsymbol{u}}_m$ is the corresponding eigenvector, and w_m is coefficient which describes how much of each eigenmode is present in the solution. Substitution of Eq. (26) into Eq. (25) gives

$$\sum_m z_m^{i-1} \left([A] + z_m[B] + z_m^2[C] \right) \{\bar{u}_m\} w_m = 0 \tag{27}$$

For this series to be zero, each term in the series must vanish so that

$$\left([A] + z_m[B] + z_m^2[C] \right) \{\bar{u}_m\} = 0 \tag{28}$$

Equation (28) is recognized as an eigenvalue problem for the eigenmodes $\bar{\boldsymbol{u}}_m$ and the corresponding eigenvalues z_m. The eigenvalue problem is put into a more conventional form by recasting Eq. (28) in state-space form, i.e.,

$$\begin{bmatrix} O & I \\ -A & -B \end{bmatrix} \begin{Bmatrix} \bar{u}_m \\ z_m \bar{u}_m \end{Bmatrix} = z_m \begin{bmatrix} I & O \\ O & C \end{bmatrix} \begin{Bmatrix} \bar{u}_m \\ z_m \bar{u}_m \end{Bmatrix} \tag{29}$$

Roughly speaking, the eigenmodes of Eq. (29) correspond to two-dimensional pressure, entropy, and vorticity waves that travel up and down the duct. The eigenvalue z_m is closely related to the axial wave number k_m of an eigenmode. By examining the eigenvalues of Eq. (29), one can determine whether the mth eigenmode is traveling away from or toward the rotor. On physical grounds, no waves should travel toward the rotor for the flutter problem since such waves would originate outside the computational domain or would be due to artificial reflections at the far-field boundary. At the upstream far-field boundary, eigenmodes with eigenvalues z_m with a magnitude less than unity represent incoming waves which decay as they move toward the rotor and hence should be excluded from the solution (the wave number k_m has a positive imaginary part). If the magnitude of the eigenvalue z_m is greater than unity, the corresponding eigenmode is an outgoing mode which decays as it moves away from the rotor (the wave number k_m has a negative imaginary part). Such waves originate from within the computational domain and are kept as part of the solution. Finally, if the magnitude of the eigenvalue is unity (the imaginary part of k_m is zero), then the direction that the wave travels is determined by its group velocity; those modes which are found to be incoming waves are to be excluded from the solution.

Figure 2 shows the eigenvalues of the upstream far-field modes of the discretized Lax-Wendroff scheme for a typical unsteady flow calculation. For this example, the blade-to-blade gap G is 1.0, the inflow Mach number M is 0.7, the inflow angle $\Omega_{-\infty}$ is 55 deg, the reduced frequency k is 1.287, and the interblade phase angle σ is -90 deg. The grid spacing between axial stations in the far field in the x and y directions is 0.0601 and 0.0716, respectively. Note that the blade geometry does not affect the far-field behavior other than to set the gap. Figure 2 also shows the eigenvalues of the continuous linearized Euler equations as they would appear in the z-plane. The eigenvalues of the discretized system agree well with the analytically determined eigenvalues for those eigenvalues near $z = (1,0)$. These eigenvalues correspond to longer wavelength (smaller interblade phase angle) modes that are well modeled by the Lax-Wendroff scheme. Computational modes with shorter wavelengths propagate with speeds and decay rates different from their corresponding analytical modes due to truncation error. Finally, note the computational eigenvalues outside the unit circle in the left-half plane. These modes are spurrows computational with no physical counterparts. In fact, one could say that all of the modes are numerical in nature; some happen to be close to physical modes (those with large wavelengths), and some do not. The goal is to eliminate all reflections of outgoing waves as they exist in the numerical scheme, whether or not they closely resemble physical modes.

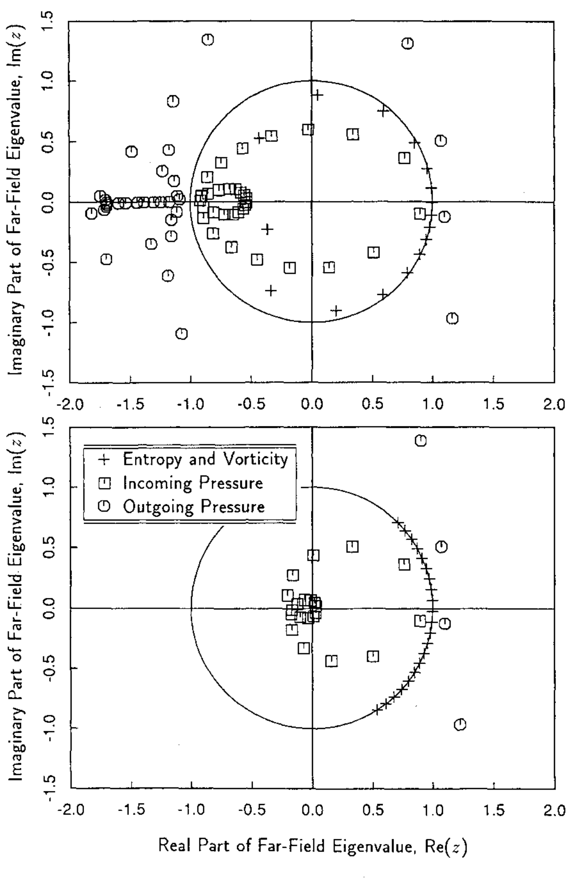

Fig. 2 Top: Eigenvalues of upstream far-field modes of discretized equations ($M_{-\infty} = 0.7$, $G = 1.0$, $\Omega_{-\infty} = 55$ deg, $k = 1.287$, $\sigma = -90$ deg, $\Delta x = 0.0601$, and $\Delta y = 0.0716$). Bottom: Analytically computed eigenvalues of far-field modes.

Consider the solution along two neighboring grid lines in the upstream far-field region (stations i and $i + 1$). Together, the solution at these two grid lines may be thought of as the state of the solution at the ith grid line. In general, this solution will contain components of all of the eigenmodes, incoming and outgoing. The state vector can be expressed in terms of the characteristic variables w as

$$\begin{Bmatrix} u_i \\ u_{i+1} \end{Bmatrix} = [E][\Lambda]^i\{w\} \tag{30}$$

where $[E]$ is the matrix of eigenvalues found by solving Eq. (29) and $[\Lambda]$ is the diagonal matrix of eigenvalues. [Equation (30) is simply Eq. (26) in vector notation.] Therefore, the state vector at the inflow boundary is related to the state vector at the second grid line by the matrix identity

$$\begin{Bmatrix} u_1 \\ u_2 \end{Bmatrix} = [E][\Lambda]^{-1}[E]^{-1} \begin{Bmatrix} u_2 \\ u_3 \end{Bmatrix} = \begin{bmatrix} T_{11} & T_{12} \\ T_{21} & T_{22} \end{bmatrix} \begin{Bmatrix} u_2 \\ u_3 \end{Bmatrix} \tag{31}$$

where $[T]$ is a transition matrix. The solution at the upstream far-field boundary is then related to the solution on the interior by

$$\{u_i\} = [T_{11} \;\; T_{12}] \begin{Bmatrix} u_2 \\ u_3 \end{Bmatrix} \tag{32}$$

The goal is to eliminate incoming waves from the solution. Hence, after each basic Lax-Wendroff iteration, the solution at the upstream boundary is found using Eq. (32). The matrices T_{11} and T_{12}, however, are constructed by first setting the entries in $[\Lambda]$ to zero that correspond to incoming modes before applying Eq. (31). This has the effect of eliminating the incoming characteristics from the solution at the inflow boundary. Note that the matrices T_{11} and T_{12} need to be computed just once before the start of the Lax-Wendroff iteration procedure. Thereafter at each iteration, the far-field nonreflecting boundary conditions require only a relatively small matrix/vector multiply.

Finally, for gust-response problems, Eq. (32) is replaced by

$$\{u_1\} = \{u_{\text{gust}}\} + [T_{11} \;\; T_{12}] \begin{Bmatrix} u_2 \\ u_3 \end{Bmatrix} \tag{33}$$

where u_{gust} is a vector composed of the desired incoming eigenmodes.

After each multiple-grid sweep, boundary conditions must also be applied to the so-called changes. These boundary conditions should be well-posed and homogeneous. Therefore, at the end of each multiple-grid sweep, we apply one-di-

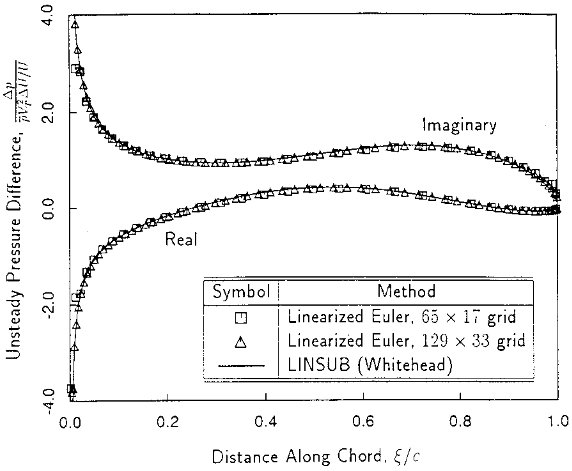

Fig. 3 Unsteady pressure difference on flat-plate cascade due to incident vortical gust ($M_{-\infty} = 0.7$, $G = 1.0$, $\Theta = 45$ deg, $\Omega_{-\infty} = 45$ deg, $k = 2.221$, and $\sigma = -180$ deg).

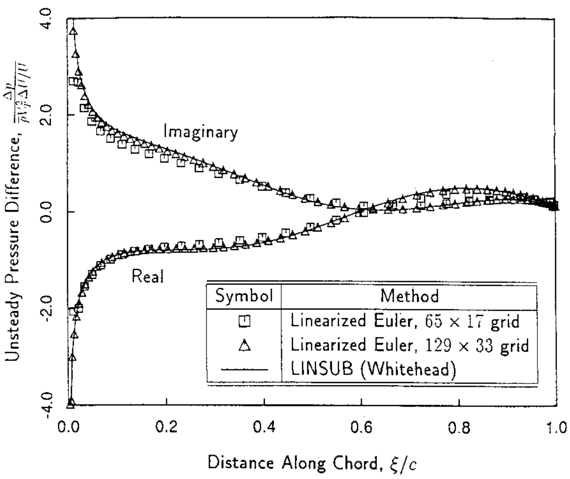

Fig. 4 Unsteady pressure difference on flat-plate cascade due to incident vortical gust ($M_{-\infty} = 0.7$, $G = 1.0$, $\Theta = 45$ deg, $\Omega_{-\infty} = 45$ deg, $k = 3.332$, and $\sigma = -270$ deg).

mensional characteristic nonreflecting boundary conditions to the changes. These boundary conditions, although reflecting at the multigrid levels, do not affect the converged solution. The overall far-field boundary treatment thus remains perfectly nonreflecting to all (two-dimensional) outgoing waves.

Numerical Results

Unsteady Flow in a Flat-Plate Cascade

To validate the present method, we computed a number of unsteady flows about a cascade of flat-plate airfoils and compared the results to those obtained from Whitehead's LINSUB code.[32,33] For all of the cases considered in this section, the mean flow through the cascade is uniform with a Mach number M of 0.7. The stagger angle Θ is 45 deg, and the gap-to-chord ratio G is 1.0.

To begin, we consider the case of an inlet distortion interacting with the flat-plate cascade. In the nonrotating frame of reference, the flow is axial with mean velocity U. The axial velocity has a sinusoidally varying deficit ΔU with an interblade phase angle σ of -180 deg. In the rotating cascade frame of reference, the airfoils thus see an unsteady gust with a reduced frequency k (based on the chord c) of 2.221. Under these conditions, the flow is superresonant; pressure waves with an interblade phase angle σ of $+180$ deg propagate in the far field. Any reflection of these pressure waves off the far-field boundaries would cause an unattenuated wave to propagate back into the computational domain, corrupting the solution. Therefore, this case provides a good test of the nonreflecting boundary conditions. Figure 3 shows the computed real and imaginary parts of the unsteady pressure difference across the surface of the reference airfoil. These results were computed on both a coarse grid (65 × 17 nodes) and a fine grid (129 × 33 nodes). For comparison, the essentially exact results from Whitehead's LINSUB code are also shown. Note that the computed solutions agree very well with the exact solution, even near the leading edge where the solution contains a square root singularity.

The next flat-plate example is for the case of an inlet distortion with an interblade phase angle σ of -270 deg and a reduced frequency k of 3.332. As seen in Fig. 4, the agreement between the linearized Euler analysis and the exact solution, although not quite as good as for the preceding case, is excellent. Furthermore, it appears from these results and from other numerical experiments performed by the authors that the present linearized Euler scheme is second-order accurate when fourth-difference smoothing is used and first-order accurate when second-difference smoothing is used.

Next, consider the case where the airfoils undergo a plunging motion with an interblade phase angle σ of -180 deg and a reduced frequency k of 2.221. Again, as shown in Fig. 5, the linearized Euler analysis is in good agreement with the exact

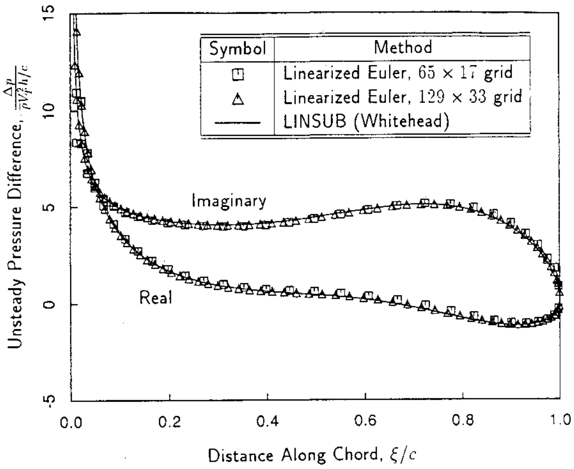

Fig. 5 Unsteady pressure difference on flat-plate cascade due to plunging motion ($M_{-\infty} = 0.7$, $\Theta = 45$ deg, $\Omega_{-\infty} = 45$ deg, $k = 2.221$, and $\sigma = -180$ deg).

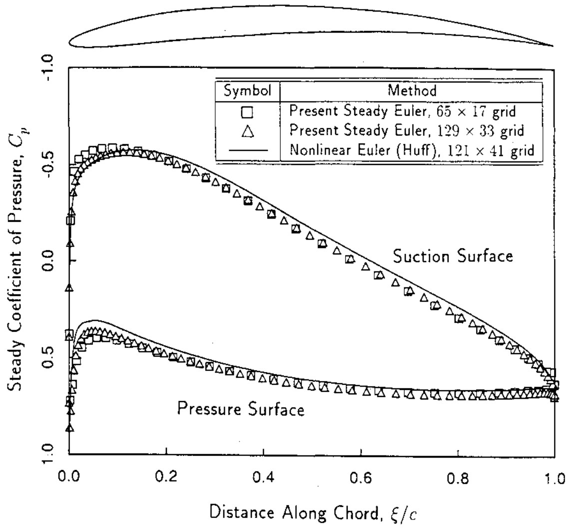

Fig. 6 Steady pressure distribution on tenth standard configuration airfoil ($M_{-\infty} = 0.7$, $G = 1.0$, $\Theta = 45$ deg, and $\Omega_{-\infty} = 55$ deg).

solution for this superresonant case. As with the gust-response examples, the leading-edge singularity is well predicted, the solution appears to be second-order accurate, and the far-field boundary conditions produce no spurious reflections.

Unsteady Subsonic Flow in a Compressor

Having demonstrated the accuracy of the method for a flat-plate geometry, we next consider unsteady flows in a more realistic compressor geometry. The purpose of these test cases is to demonstrate the method's ability to compute accurately the unsteady flow over loaded airfoils, the computational efficiency of the method, and the effectiveness of the far-field boundary conditions.

The cascade considered in this section is the tenth standard configuration,[34] which is a cascade of cambered airfoils with a slightly modified NACA 0006 thickness distribution. The airfoil has a circular arc camber distribution with a maximum height of 5 percent of the chord. The stagger angle Θ is 45 deg and the gap-to-chord ratio G is 1.0. The mean inflow angle $\Omega_{-\infty}$ is 55 deg and the inflow Mach number $M_{-\infty}$ is 0.7. Figure 6 shows the mean flow surface pressure calculated using the present steady nonlinear Euler solver as well as an Euler solver developed by Huff[6] that uses a flux difference splitting algorithm. For the case considered here, the maximum Mach number on the suction surface is about 0.92.

Having computed the steady flow through the blade row, the unsteady flow due to a steady inlet distortion in the stator frame of reference is computed. For this example, the interblade phase angle σ is -90 deg and the reduced frequency k is 1.287 corresponding to a disturbance with a wavelength in the circumferential direction of four blade-to-blade gaps. In the stationary frame of reference, the total enthalpy is constant. Figure 7 shows the calculated unsteady pressure distribution. The good agreement between the coarse grid and the fine grid solutions shows that the fine grid solution is nearly grid converged. Also shown is the solution computed using a

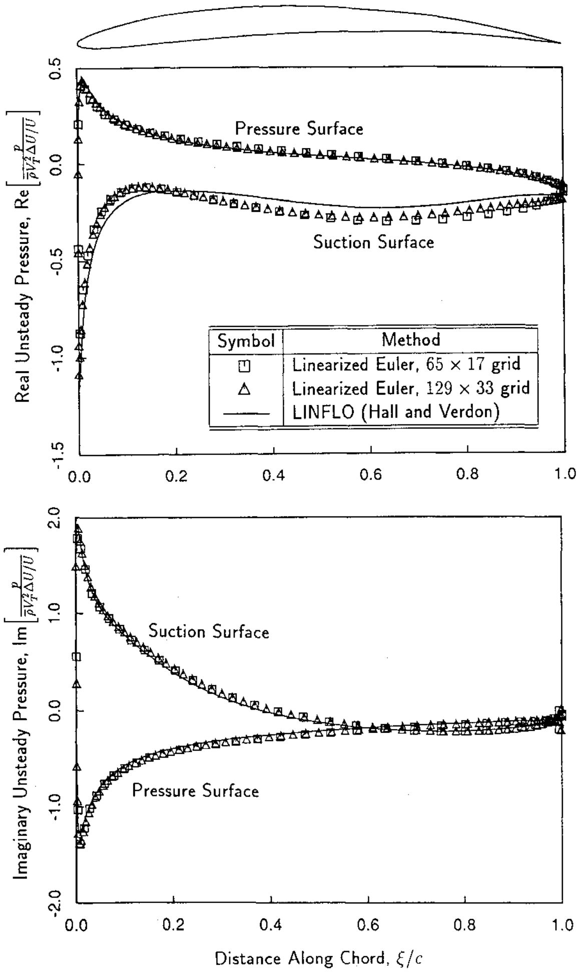

Fig. 7 Unsteady pressure distribution on tenth standard configuration airfoil due to an incident vortical gust ($M_{-\infty} = 0.7$, $k = 1.287$, and $\sigma = -90$ deg).

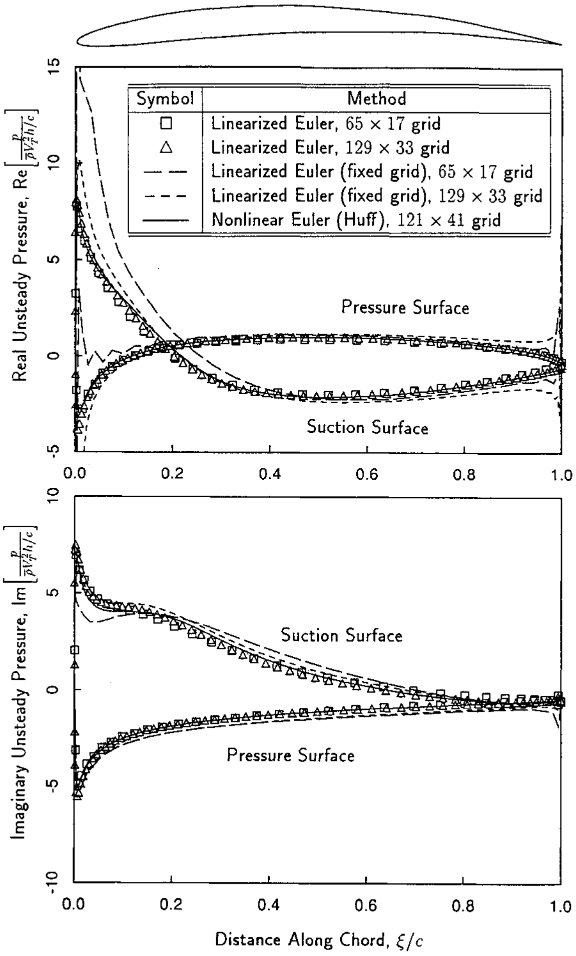

Fig. 8 Unsteady pressure distribution on tenth standard configuration airfoil due to plunging motion ($M_{-\infty} = 0.7$, $k = 1.287$, and $\sigma = -90$ deg).

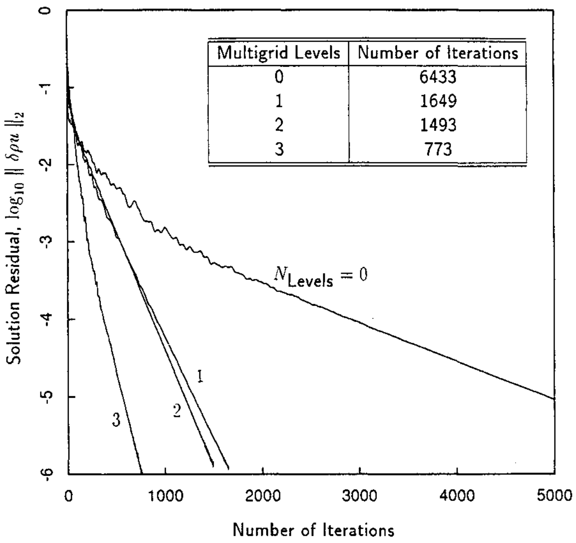

Fig. 9 Convergence histories for gust-response calculations using different numbers of multiple-grid levels, N_{Levels}.

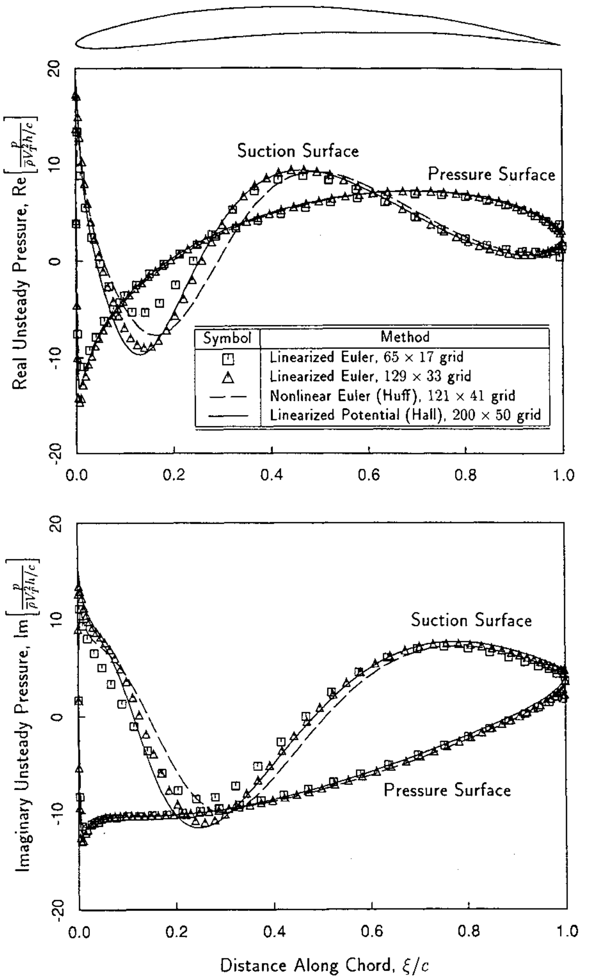

Fig. 10 Unsteady pressure distribution on tenth standard configuration airfoil due to plunging motion ($M_{-\infty} = 0.7$, $k = 2.573$, and $\sigma = -180$ deg).

linearized potential code (LINFLO).[16] The overall agreement with the LINFLO analysis is good although there is a slight discrepancy in the real part on the suction surface.

Next, we consider unsteady plunging motion of the compressor blades. For the first example the blades vibrate with an interblade phase angle σ of -90 deg and a reduced frequency k of 1.287. Figure 8 shows the unsteady pressure distribution on the surface of the reference airfoil found using the present linearized Euler analysis and the nonlinear time-marching Euler analysis of Huff. Note that the coarse and fine grid solutions are in excellent agreement with one another and also with the nonlinear Euler solution.

Also shown in Fig. 8 are linearized Euler solutions calculated on fixed (i.e., nondeforming) computational grids. For these solutions, extrapolation terms which depend on mean flow gradients must be added to the airfoil boundary conditions and to the expression for the unsteady surface pressure to account for the fact that the airfoil vibrates through the stationary grid. Large errors are seen in the solutions computed on the fixed grid, especially around the leading and trailing edges. These errors are inevitable when using a fixed grid due to the difficulty in evaluating the gradient of the mean flowfield near the airfoil surface.

Figure 9 shows the convergence histories for the preceding (deforming grid) calculation on the coarse grid using the basic Lax-Wendroff solver along and with Ni's multiple-grid acceleration technique.[30] Without the multiple-grid accelerator, the linearized unsteady Euler analysis required 6433 iterations to converge. With three levels of the multiple-grid accelerator, the analysis required just 773 iterations, corresponding to about 14 min of computer time on a Stardent 3000 workstation. The nonlinear time-marching solution, on the other hand, required 7384 iterations and approximately 88 min on a CRAY-YMP. When also taking into consideration the difference in speeds of the two computers, one concludes that the linearized Euler analysis is nearly two orders of magnitude faster than the nonlinear analysis while still modeling the essential features of the unsteady flow.

Finally, we consider a moderately high reduced frequency blade motion case to demonstrate the limitations of the present method. For this case, the airfoils vibrate in plunge with an interblade phase angle σ of -180 deg and a reduced frequency k of 2.573. Figure 10 shows the computed surface pressure distribution. Also shown for comparison are the results of a linearized potential analysis[26] and a time-marching Euler calculation. The potential solution, which was computed on an extremely fine grid (200×50 nodes), is grid converged. The fine grid linearized Euler calculation is in very good agreement with the potential calculation. The coarse grid linearized Euler calculation, on the other hand, differs significantly from the potential solution on the suction surface. On

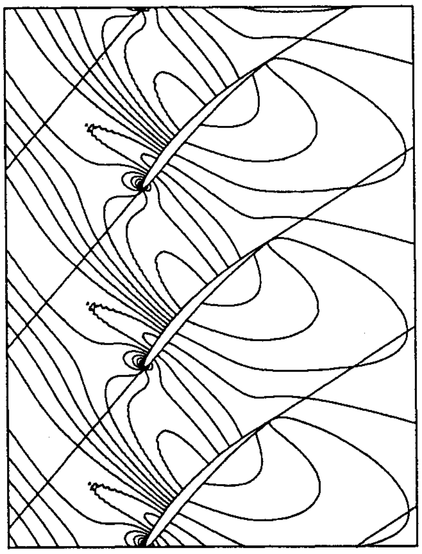

Fig. 11 Contours of unsteady pressure for cascade of plunging tenth standard configuration airfoils ($M_{-\infty} = 0.7$, $k = 2.573$, and $\sigma = -180$ deg).

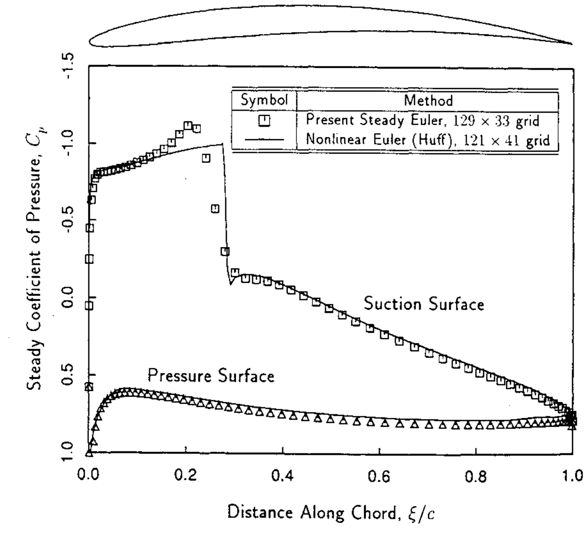

Fig. 12 Steady pressure distribution on tenth standard configuration airfoil ($M_{-\infty} = 0.8$, $G = 1.0$, $\Theta = 45$ deg, and $\Omega_{-\infty} = 58$ deg).

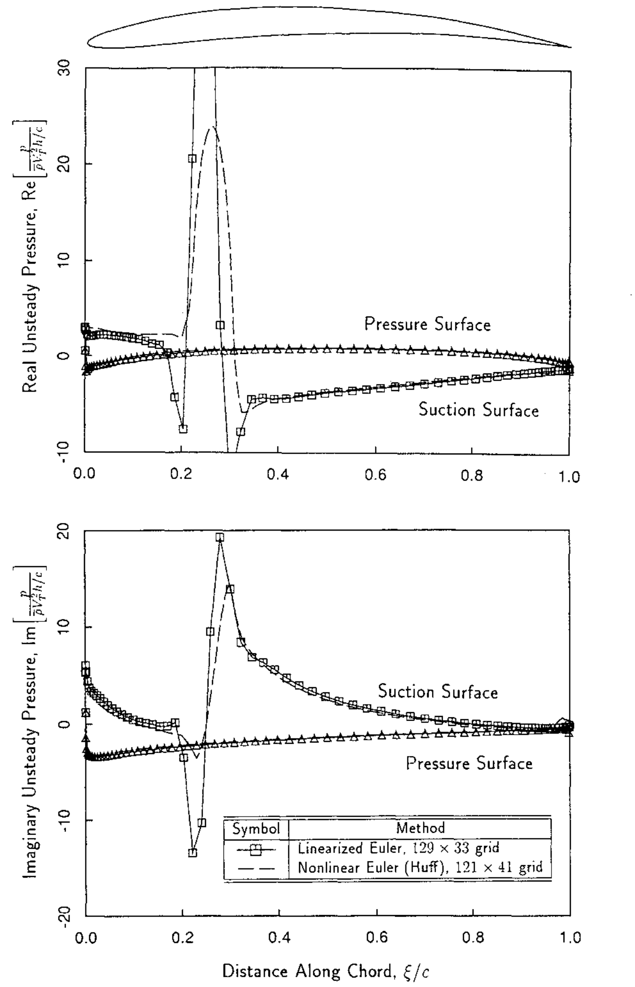

Fig. 13 Unsteady pressure distribution on tenth standard configuration airfoil due to plunging motion ($M_{-\infty} = 0.8$, $k = 1.287$, and $\sigma = -90$ deg).

the suction surface, where the Mach number is large, upstream traveling pressure disturbances have very short wavelengths that are difficult to resolve. Of course, adequate grid resolution is essential for both nonlinear and linearized analyses. We suspect that the discrepancy between the linearized Euler and nonlinear Euler solutions is due in part to the fairly coarse grid used to obtain the nonlinear Euler solution.

Figure 11 shows the unsteady pressure contours for this blade-motion case. Of particular interest is the behavior of the solution in the far-field region. For this example the flow is superresonant upstream and subresonant downstream. In both the upstream and downstream far-field regions, the pressure contours are seen to pass smoothly out of the computational domain without reflection, demonstrating the effectiveness of the far-field nonreflecting boundary conditions.

Unsteady Transonic Flow in a Compressor

To demonstrate the transonic capabilities of the present analysis, we again consider the tenth standard configuration compressor cascade. The upstream Mach number $M_{-\infty}$ is now 0.8 and the inflow angle $\Omega_{-\infty}$ is 58 deg. Figure 12 shows the computed steady pressure distribution. Note in particular the transonic patch on the suction surface of the airfoil. The present steady Euler solver captures the resulting shock over about five grid points. Also shown is the nonlinear Euler solutions of Huff. Note the sharp shock definition afforded by the flux difference splitting scheme.

Figure 13 shows the computed unsteady pressure distribution for the case where the blades vibrate in plunge with an interblade phase angle σ of -90 deg and a reduced frequency k of 1.287. The agreement between the linearized analysis and the nonlinear time-marching Euler analysis is excellent, demonstrating the ability of the present analysis to model accurately transonic flows. Of particular interest is the "shock impulse" seen on the suction surface. The area of this impulse represents the unsteady load acting on the airfoil due to the unsteady motion of the shock. Although the widths of the shock impulses predicted by the linearized and nonlinear Euler solvers is somewhat different, the integrated areas of the impulses are approximately equal.

Concluding Remarks

This paper has presented a linearized unsteady Euler analysis suitable for analysis of the aerodynamic loads in turbomachinery blade rows arising from both incident gusts and unsteady blade motion. Linear variable-coefficient equations describe the unsteady small-perturbation flow. These equations have a similar form to the nonlinear Euler equations and are solved very efficiently using a multiple-grid Lax-Wendroff algorithm. For blade-motion problems, the use of a harmonically deforming grid eliminates mean flow gradient terms from the flow tangency boundary condition and unsteady surface pressure evaluation, dramatically improving the accuracy of the method. Another important feature of the present analysis is the treatment of the far field. Eigenmodes, found from an eigenanalysis of the far-field discretized equations, are used to construct numerically exact nonreflecting boundary conditions.

Several flat-plate test cases were presented, and the computed results agreed well with exact solutions. Comparisons of computed unsteady subsonic and transonic flows about a cascade of compressor blades to a nonlinear time-marching Euler analysis demonstrate the ability of the present method to predict accurately unsteady aerodynamic forces on loaded airfoils operating at moderate reduced frequencies. Furthermore, typical unsteady flow calculations require a fraction of the computational time required to perform similar calculations using nonlinear time-marching techniques, making the present analysis an ideal engineering design tool.

Acknowledgments

This work was supported by the NASA Lewis Research Center, NASA Grant NAG3-1192, with Daniel Hoyniak serving as technical monitor.

References

[1] Hodson, H. P., "An Inviscid Blade-to-Blade Prediction of a Wake Generated Unsteady Flow," American Society of Mechanical Engineers, Paper 84-GT-43, 1984.

[2] Fourmaux, A., and Le Meur, A., "Computation of Unsteady Phenomena in Transonic Turbines and Compressors," presented at the Fourth Symposium on Unsteady Aerodynamics and Aeroelasticity of Turbomachines and Propellers, Aachen Univ. of Technology, Aachen, Germany, Sept. 6-10, 1987.

[3] Whitfield, D. L., Swafford, T. W., and Mulac, R. A., "Three-Dimensional Unsteady Euler Solutions for Propfans and Counter-Rotating Propfans in Transonic Flow," AIAA 19th Fluid Dynamics, Plasma Dynamics, and Lasers Conference, AIAA Paper 87-1197, Honolulu, HI, June 8-10, 1987.

[4] Giles, M. B., "Calculation of Unsteady Wake/Rotor Interaction," *Journal of Propulsion and Power,* Vol. 4, No. 4, 1988, pp. 356-362.

[5] He, L., "An Euler Solution for Unsteady Flows Around Oscillating Blades," *Transactions of the ASME Journal of Turbomachinery,* Vol. 112, No. 4, 1990, pp. 714-722.

[6] Huff, D. L., Swafford, T. W., and Reddy, T. S. R., "Euler Flow Predictions for an Oscillating Cascade Using a High Resolution Wave-Split Scheme," American Society of Mechanical Engineers, International Gas Turbine and Aeroengine Congress and Exposition, Paper 91-GT-198, Orlando, FL, June 3-6, 1991.

[7] Rai, M. M., "Three-Dimensional Navier-Stokes Simulations of Turbine Rotor-Stator Interaction; Pt. I—Methodology," *Journal of Propulsion and Power,* Vol. 5, No. 3, 1989, pp. 307-311.

[8]Rai, M. M., "Three-Dimensional Navier-Stokes Simulations of Turbine Rotor-Stator Interaction; Pt. II—Results," *Journal of Propulsion and Power,* Vol. 5, No. 3, 1989, pp. 312–319.

[9]Abhari, R. S., Guenette, G. R., Epstein, A. H., and Giles, M. B., "Comparison of Time-Resolved Turbine Rotor Heat Transfer Measurements and Numerical Calculations," American Society of Mechanical Engineers, International Gas Turbine and Aeroengine Congress and Exposition, Paper 91-GT-268, Orlando, FL, June 3–6, 1991.

[10]Giles, M. B., and Haimes, R., "Validation of a Numerical Method for Unsteady Flow Calculations," American Society of Mechanical Engineers, International Gas Turbine and Aeroengine Congress and Exposition, Paper 91-GT-271, Orlando, FL, June 3–6, 1991.

[11]Verdon, J. M., Adamczyk, J. J., and Caspar, J. R., "Subsonic Flow Past an Oscillating Cascade with Steady Blade Loading—Basic Formulation," *Unsteady Aerodynamics,* edited by R. B. Kinney, Univ. of Arizona, Tucson, AZ, July 1975, pp. 827–851.

[12]Verdon, J. M., and Caspar, J. R., "Development of a Linear Unsteady Aerodynamic Analysis for Finite-Deflection Subsonic Cascades," *AIAA Journal,* Vol. 20, No. 9, 1982, pp. 1259–1267.

[13]Verdon, J. M., and Casper, J. R., "A Linearized Unsteady Aerodynamic Analysis for Transonic Cascades," *Journal of Fluid Mechanics,* Vol. 149, Dec. 1984, pp. 403–429.

[14]Verdon, J. M., "Linearized Unsteady Aerodynamic Theory," *AGARD Manual on Aeroelasticity in Axial-Flow Turbomachines, Unsteady Turbomachinery Aerodynamics,* edited by M. F. Platzer and F. O. Carta, AGARD-AG-298, Vol. 1, Neuilly sur Seine, France, March 1987.

[15]Whitehead, D. S., and Grant, R. J., "Force and Moment Coefficients of High Deflection Cascades," *Proceedings of the 2nd International Symposium on Aeroelasticity in Turbomachines,* edited by P. Suter, Juris-verlag Zurich, 1981, pp. 85–127.

[16]Hall, K. C., and Verdon, J. M., "Gust Response of a Cascade Operating in a Nonuniform Mean Flow," AGARD Propulsion and Energetics Panel 74th Specialists' Meetings on Unsteady Aerodynamic Phenomena in Turbomachines, Kirchberg Plateau, Luxembourg, Aug. 28–Sept. 1, 1989.

[17]Caruthers, J. E., and Dalton, W. N., "Unsteady Aerodynamic Response of a Cascade to Nonuniform Inflow," American Society of Mechanical Engineers, International Gas Turbine and Aeroengine Congress and Exposition, Paper 91-GT-174, Orlando, FL, June 3–6, 1991.

[18]Atassi, H. M., and Grzedzinski, J., "Unsteady Disturbances of Streaming Motions Around Bodies," *Journal of Fluid Mechanics,* Vol. 209, Dec. 1989, pp. 504–513.

[19]Ni, R. H., and Sisto, F., "Numerical Computation of Nonstationary Aerodynamics of Flat Plate Cascades in Compressible Flow," *Transactions of the ASME, Journal of Engineering for Power,* Vol. 98, April 1976, pp. 165–170.

[20]Hall, K. C., and Crawley, E. F., "Calculation of Unsteady Flows in Turbomachinery Using the Linearized Euler Equations," *AIAA Journal,* Vol. 27, No. 6, 1989, pp. 777–787.

[21]Lindquist, D. R., and Giles, M. B., "On the Validity of Linearized Unsteady Euler Equations with Shock Capturing," *Proceedings of the AIAA 10th Computational Fluid Dynamics Conference* (Honolulu, HI), AIAA, Washington, DC, June 1991 (AIAA Paper 91-1598-CP).

[22]Bendiksen, O. O., and Kousen, K. A., "Transonic Flutter Analysis Using the Euler Equations," AIAA Paper 87–1238, June 1987.

[23]Venkatakrishnan, V., and Jameson, A., "Computation of Unsteady Transonic Flows by the Solution of Euler Equations," *AIAA Journal,* Vol. 26, No. 8, 1988, pp. 974–981.

[24]Rausch, R. D., Batina, J. T., and Yang, H. T. Y., "Euler Flutter Analysis of Airfoils Using Unstructured Dynamic Meshes," *Proceedings of the AIAA/ASME/ASCE/AHS/ASC 30th Structures, Structural Dynamics and Materials Conf*erence (Mobile, AL), Washington, DC, April 1989 (AIAA Paper 89-1384).

[25]Batina, J. T., "Unsteady Euler Algorithm with Unstructured Dynamic Mesh for Complex-Aircraft Aeroelastic Analysis," AIAA Paper 89-1189-CP, April 1989.

[26]Hall, K. C., "A Deforming Grid Variational Principle and Finite Element Method for Computing Unsteady Small Disturbance Flows in Cascades," AIAA 30th Aerospace Sciences Meeting, AIAA Paper 92-0665, Reno, NV, Jan. 6–9, 1992.

[27]Hall, K. C., and Lorence, C. B., "Calculation of Three-Dimensional Unsteady Flows in Turbomachinery Using the Linearized Harmonic Euler Equations," American Society of Mechanical Engineers, 37th International Gas Turbine and Aeroengine Congress and Exposition, Paper 92-GT-136, Cologne, Germany, June 1–4, 1992.

[28]Van Dyke, M., *Perturbation Methods in Fluid Mechanics,* Academic, New York, 1964, pp. 99–120.

[29]Thompson, J. F., Thames, F. C., and Mastin, W., "A Code for Numerical Generation of Boundary-Fitted Curvilinear Coordinate Systems on Fields Containing any Number of Arbitrary Two-Dimensional Bodies," *Journal of Computational Physics,* Vol. 24, No. 3, 1977, pp. 274–302.

[30]Ni, R. H., "A Multiple-Grid Scheme for Solving the Euler Equations," *AIAA Journal,* Vol. 20, No. 11, 1982, pp. 1565–1571.

[31]Dannenhoffer, J. D., III, "Grid Adaptation for Complex Two-Dimensional Transonic Flows," Sc.D. Thesis, Dept. of Aeronautics and Astronautics, Massachusetts Inst. of Technology, Cambridge, MA, Aug. 1987.

[32]Whitehead, D. S., "Classical Two-Dimensional Methods," *AGARD Manual on Aeroelasticity in Axial-Flow Turbomachines, Unsteady Turbomachinery Aerodynamics,* edited by M. F. Platzer and F. O. Carta, Vol. 1, AGARD-AG-298, Neuilly sur Seine, France, March 1987.

[33]Smith, S. N., "Discrete Frequency Sound Generation in Axial Flow Turbomachines," Aeronautical Research Council, Reports and Memoranda 3709, London, March 1972.

[34]Fransson, T. H., private communication, Laboratoire de Thermique appliqueé et Turbomachines, Ecole Polytechnique Federale de Lausanne, Lausanne, Switzerland, June 1991.